12th AIAA/CEAS Aeroacoustics Conference (27th AIAA Aeroacoustics Conference)
8 - 10 May 2006, Cambridge, Massachusetts

AIAA 2006-2503

Direct Noise Computation around a 3-D NACA 0012 airfoil

Olivier Marsden*, Christophe Bogey†, Christophe Bailly‡

A Large Eddy Simulation of the flow around a NACA 0012 airfoil at a Reynolds number of 500,000 is presented. At this Reynolds number, the boundary layers transition from an initially laminar state to a turbulent state before reaching the trailing edge. Results obtained in this LES show a well-placed transition zone, and turbulence levels in good agreement with experimental data. Furthermore, the radiated acoustic field is computed directly in the same computation, which should allow future detailed examinations of the noise radiated by such a flow configuration.

I. Introduction

Recent rapid advances in Computational Aeroacoustics (CAA) have greatly increased the scope of problems that can be tackled by numerical methods. This is particularly true of Direct Noise Computations (DNC), in which the sound waves generated by turbulent flows are obtained directly from an unsteady compressible simulation of the Navier-Stokes equations. Indeed, high-Reynolds-number flows are now increasingly attainable, thanks to the development of high-order LES simulations that manage to preserve the large-scale small-amplitude acoustic perturbations alongside the small-scale large-amplitude aerodynamic fluctuations. The field of jet aeroacoustics has been particularly active in the advancement of these techniques, and a number of high-Reynolds-number jet flow simulations can be found in the literature.[2,5,6,29] More recently, work on high-accuracy computations around curved geometries has shown that these methods are not restricted to Cartesian simulations.[21,22,26,27,30] A small number of time-accurate numerical studies has been performed around airfoils, generally placed at a small angle of attack to the flow, using an acoustic analogy to obtain far-field sound characteristics.[17,21,25,31] The current work describes the use of a parallel curvilinear solver, based on high-order methods, to study the compressible flow around a 3-D NACA 0012 airfoil at a chord-based Reynolds number of 500,000, placed parallel to the upstream flow. It focuses on showing that realistic boundary layer transition is captured without needing to trigger the transition artificially, even when the airfoil is parallel to the upstream flow. Both mean flow quantities as well as fluctuation statistics compare well with experimental data. The acoustic field generated by the airfoil is also examined.

II. Numerical aspects

High-order Navier-Stokes simulations having proven their value in the study of noise-generation mechanisms in both free jet flows[6] and rectangular cavity flows,[13] we are developing similar methods for more complex curved geometries.

The full 3-D Navier-Stokes equations are solved on a structured computational grid which is obtained from a body-fitted C-type grid by applying a suitable coordinate transform. The geometrical transform is characterized by its Jacobian matrix, which describes the variations of the computational coordinates ξ, η and ζ

*Research associate, Department of Engineering, University of Cambridge
†Research scientist, Laboratoire de Mécanique des Fluides et d'Acoustique, Ecole Centrale de Lyon, UMR CNRS 5509, 69134 Ecully, France
‡Professor, Laboratoire de Mécanique des Fluides et d'Acoustique, Ecole Centrale de Lyon

as a function of the physical coordinates x, y and z, is given by

$$J = \begin{vmatrix} \frac{\partial \xi}{\partial x} & \frac{\partial \eta}{\partial x} & \frac{\partial \zeta}{\partial x} \\ \frac{\partial \xi}{\partial y} & \frac{\partial \eta}{\partial y} & \frac{\partial \zeta}{\partial y} \\ \frac{\partial \xi}{\partial z} & \frac{\partial \eta}{\partial z} & \frac{\partial \zeta}{\partial z} \end{vmatrix}$$

The transformed equations can be written as follows:

$$\begin{aligned} \frac{\partial}{\partial t}\left(\frac{\mathbf{U}}{J}\right) &+ \frac{\partial}{\partial \xi}\left\{\frac{1}{J}\left[\xi_x(\mathbf{E_e}-\mathbf{E_v})+\xi_y(\mathbf{F_e}-\mathbf{F_v})+\xi_z(\mathbf{G_e}-\mathbf{G_v})\right]\right\} \\ &+ \frac{\partial}{\partial \eta}\left\{\frac{1}{J}\left[\eta_x(\mathbf{E_e}-\mathbf{E_v})+\eta_y(\mathbf{F_e}-\mathbf{F_v})+\eta_z(\mathbf{G_e}-\mathbf{G_v})\right]\right\} \\ &+ \frac{\partial}{\partial \zeta}\left\{\frac{1}{J}\left[\zeta_x(\mathbf{E_e}-\mathbf{E_v})+\zeta_y(\mathbf{F_e}-\mathbf{F_v})+\zeta_z(\mathbf{G_e}-\mathbf{G_v})\right]\right\} = 0 \end{aligned} \tag{1}$$

where

$$\mathbf{U} = (\rho, \rho u, \rho v, \rho w, \rho e_t)^T \tag{2}$$

and the inviscid and visco-thermal fluxes are given respectively by:

$$\mathbf{E_e} = \begin{pmatrix} \rho u \\ \rho u^2 + p \\ \rho uv \\ \rho uw \\ (\rho e_t + p)u \end{pmatrix} \quad \mathbf{E_v} = \begin{pmatrix} 0 \\ \tau_{xx} \\ \tau_{xy} \\ \tau_{xz} \\ u\tau_{xx} + v\tau_{xy} + w\tau_{xz} - q_x \end{pmatrix}$$

$$\mathbf{F_e} = \begin{pmatrix} \rho v \\ \rho uv \\ \rho v^2 + p \\ \rho vw \\ (\rho e + p)v \end{pmatrix} \quad \mathbf{F_v} = \begin{pmatrix} 0 \\ \tau_{xy} \\ \tau_{yy} \\ \tau_{yz} \\ u\tau_{xy} + v\tau_{yy} + w\tau_{yz} - q_y \end{pmatrix}$$

$$\mathbf{G_e} = \begin{pmatrix} \rho w \\ \rho uw \\ \rho vw \\ \rho w^2 + p \\ (\rho e + p)w \end{pmatrix} \quad \mathbf{G_v} = \begin{pmatrix} 0 \\ \tau_{xz} \\ \tau_{yz} \\ \tau_{zz} \\ u\tau_{xz} + v\tau_{yz} + w\tau_{zz} - q_z \end{pmatrix}$$

The shear stress terms are given by the following expressions:

$$\begin{aligned}
\tau_{xx} &= \tfrac{2}{3}\mu[2(\xi_x u_\xi + \eta_x u_\eta + \zeta_x u_\zeta) - (\xi_y v_\xi + \eta_y v_\eta + \zeta_y v_\zeta) - (\xi_z w_\xi + \eta_z w_\eta + \zeta_z w_\zeta)] \\
\tau_{yy} &= \tfrac{2}{3}\mu[2(\xi_y v_\xi + \eta_y v_\eta + \zeta_y v_\zeta) - (\xi_x u_\xi + \eta_x u_\eta + \zeta_x u_\zeta) - (\xi_z w_\xi + \eta_z w_\eta + \zeta_z w_\zeta)] \\
\tau_{zz} &= \tfrac{2}{3}\mu[2(\xi_z w_\xi + \eta_z w_\eta + \zeta_z w_\zeta) - (\xi_x u_\xi + \eta_x u_\eta + \zeta_x u_\zeta) - (\xi_y v_\xi + \eta_y v_\eta + \zeta_y v_\zeta)] \\
\tau_{xy} &= \mu(\xi_y u_\xi + \eta_y u_\eta + \zeta_y u_\zeta + \xi_x v_\xi + \eta_x v_\eta + \zeta_x v_\zeta) \\
\tau_{xz} &= \mu(\xi_z u_\xi + \eta_z u_\eta + \zeta_z u_\zeta + \xi_x w_\xi + \eta_x w_\eta + \zeta_x w_\zeta) \\
\tau_{yz} &= \mu(\xi_z v_\xi + \eta_z v_\eta + \zeta_z v_\zeta + \xi_y w_\xi + \eta_y w_\eta + \zeta_y w_\zeta) \\
q_x &= -k(\xi_x T_\xi + \eta_x T_\eta + \zeta_x T_\zeta) \\
q_y &= -k(\xi_y T_\xi + \eta_y T_\eta + \zeta_y T_\zeta) \\
q_z &= -k(\xi_z T_\xi + \eta_z T_\eta + \zeta_z T_\zeta)
\end{aligned}$$

where the heat flux terms q_x, q_y and q_z are obtained thanks to Fourier's law:

$$\mathbf{q} = -k\nabla T$$

where $k = \mu c_p/\sigma$, μ is the dynamic molecular viscosity, c_p the specific heat at constant pressure and σ, Prandtl's number, whose value is generally set to 0.72 for typical air flows.

The transformed compressible Navier-Stokes equations are resolved on the computational grid with an optimised high-order numerical procedure. Away from boundaries, spatial discretization is performed with explicit eleven-point centred finite differences optimised to minimize dispersion, and filtering is done with an explicit eleven-point centred sharp-cutoff filter that damps scales discretized by fewer than four points per wavelength. Close to boundaries, be they solid walls or radiation conditions, optimised non-centred differencing schemes and filters are used. The non-centred differencing schemes are also all based on eleven-point stencils, including the one-sided stencil used for wall points. Filters for grid points more than two points away from a boundary are also built on eleven-point stencils, while the last point and last but next point stencils up to two points away from a boundary are built respectively on four and seven points. Time integration is performed with a six-step second-order optimised low-storage Runge-Kutta algorithm. Characteristics regarding dispersion and dissipation for the spatial differencing schemes, filters, and the time integration scheme can be found in.[1,4,5] This solver has been validated on reference flow configurations and on a demanding multi-body acoustic scattering test-case, yielding results in excellent agreement with experimental and analytical data.[22]

The schemes' properties mean that the behaviour of waves discretized by at least four points per wavelength is accurately reproduced, with very low levels of dispersion and dissipation, for combinations of frequency and time step respecting $\omega\Delta t \leq 1.25 \times \pi$. The airfoil wall is modeled as an isothermal non-slip boundary. The non-slip boundary condition used in this work is based entirely on the use of high-order non-centred differencing stencils and corresponding filters: the wall-point density and pressure is updated by resolving the Navier-Stokes equations in which all terms containing wall velocities are eliminated. The non-centred differencing schemes are unstable for very high frequencies, and it is therefore essential to use them in conjunction with appropriate highly selective filters. To this end, we use the filters described in Berland *et al.*[1] This boundary condition approach is inherently capable of dealing with meshes that are not orthogonal to the wall boundary, and thus reduces potential orthogonality problems near the trailing edge. At radiation boundaries, a three-dimensional generalization of Tam and Dong's 2D radiation condition[28] is used. Details on the 3D formulation can be found in Bogey and Bailly.[3] The boundary condition in the spanwise direction is chosen to be periodic, and is implemented in such a way as to allow the use of the

eleven-point differentiation and filter stencils right up to the lateral boundaries.
The approach followed for dealing with sub-grid scales in this work is to remove the energy associated with unsupported length scales thanks to the explicit filtering described above. This filtering procedure is designed to have a negligible effect on scales discretized by at least four points per wavelength. The validity of this sub-grid-scale approach is described in detail in Bogey & Bailly (2005).[5]

Parallelization of the code is based on the MPI interface. The computational domain is split along the radial and circumferential directions, resulting in a number of structured sub-grids that communicate along their shared boundaries at each sub-iteration of the Runge-Kutta time integration procedure. No dynamic load balancing is performed, but given the structure of the code, an equal number of points in each zone leads to reasonably similar computational costs for each zone. Communication is performed such that the eleven-point differencing scheme and filters can be applied transparently and in a time-accurate manner[14] right up to each lateral boundary. An evaluation of the communication overheads performed on a cluster of ALPHA EV7 processors with a high-speed infiniband^{TM}interconnect showed that communication overheads remained under 5% of the total computational time for the grid used in this work and for numbers of processors ranging up to 126.

The computation presented here has been performed on a 12.3-million point grid, composed of 1193 points in the circumferential direction, 230 points in the radial direction and 45 points in the spanwise direction. The computational domain is split into 13 subdomains and the parallel computation was run on a laboratory cluster of 13 opteron processors.
Grid resolution is important for such a simulation, if one is to capture the detailed boundary layer behaviour without using wall models. Indeed, various studies[8–10,24] have shown that low grid resolution leads to poor computational results when transitional phenomena are present. Furthermore, different SGS modelings tend to show widely varying results on under-resolved transitional zones. Therefore, in this work, care is taken to ensure that near-wall grid resolution is satisfactory. Grid spacings in wall units close to the trailing edge are as follows: $x^+ \simeq 20$, $y^+ \simeq 2.5$, and $z^+ \simeq 20$. The total computational domain extends out approximately one chordlength in the radial direction, and half a chordlength beyond the trailing edge in the downstream direction. A sponge zone is implemented in the last twenty points of the wake zone to minimize the force of vortical structures impinging on the downstream radiation condition. The effect of the sponge zone can also be noticed on the acoustic field shown in Figure (11) where acoustic waves seem to disappear in the downstream direction after $x/c \simeq 1.25$. This is in fact just an effect of the increased numerical dissipation in the sponge zone.

III. Results

A preliminary examination of the computational results shows them to be free from gross artifacts such as those sometimes induced by radiation conditions, especially given the proximity of the radiation conditions to the acoustic source zone. The boundary radiation formulation supposes a uniform mean flow, which is not the case in the computation, so the absence of large-scale reflections or other problems is in itself positive.
The pressure distribution around the airfoil is an important parameter, both in terms of aerodynamic characteristics, since it determines the lift and drag coefficients of the airfoil, and in terms of boundary layer behaviour, since the pressure gradient is known to affect the development of both laminar and turbulent boundary layers.[7,12,20] This distribution is shown in Figure (1), and is compared with experimental values obtained by Lee and Kang[18,19] for a NACA 0012 airfoil at a Reynolds number of 600,000. An excellent agreement is found between the computational and experimental results. Of importance is the fact that from $x/c = 0.15$ down to the trailing edge, the boundary layer is subject to an adverse pressure gradient.

Results concerning the boundary layer transition from a laminar to a turbulent state are now examined. It should be noted that transition is a very sensitive flow phenomenon, and as such can be strongly affected by experimental conditions, for example the level of free-stream turbulence.[11,15] Thus experimental results regarding transition show spread, and qualitative agreement between the computation and experimental results would already be positive.

A first illustration of the boundary layer behaviour is shown in Figure (2). Profiles of mean velocity normalized by the free-stream velocity are plotted at different points along the chord, and show the progressive evolution from a laminar boundary layer until $x/c = 0.55$, characterized by a linear increase in velocity over most of the boundary thickness, to a turbulent boundary layer from about $x/c = 0.75$ onwards, for which two clearly distinct zones can be observed. The shape factor at the trailing edge is found to be $H = \delta^*/\delta_\theta \simeq 1.7$.

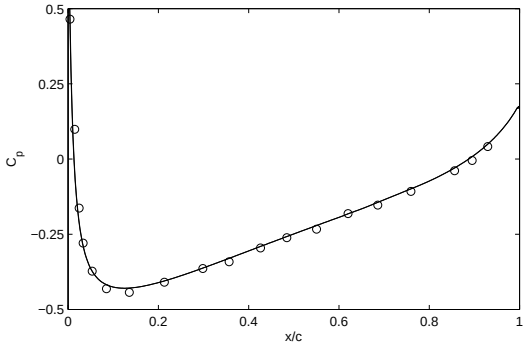

Figure 1. Mean pressure coefficient $C_p = (p - p_\infty)/(0.5\rho u_\infty^2)$ around a NACA0012 airfoil. ∘ airfoil at $\mathbf{Re}_c = 600,000$ (measurements by Lee and Kang[18]), — simulation at $\mathbf{Re}_c = 500,000$ and M= 0.22.

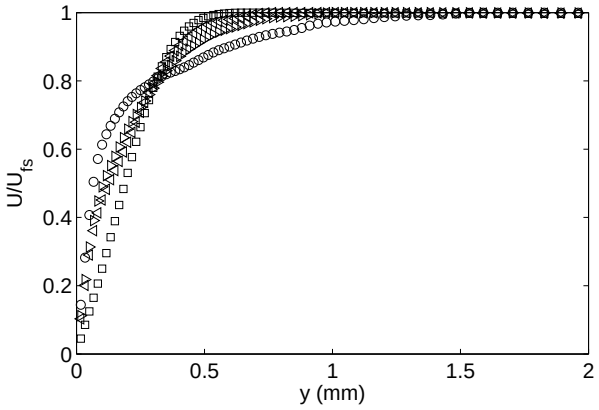

Figure 2. Mean velocity profiles u/U_∞ at different points along the chord in the upper boundary layer around a NACA0012 airfoil at $\mathbf{Re}_c = 500,000$ and M= 0.22. Computational results: □ $x/c = 0.52$, ◁ $x/c = 0.59$, ▷ $x/c = 0.63$, ∘ $x/c = 0.71$.

Figure (3) gives a better illustration of the two regions in the turbulent boundary layer, by representing the velocity profiles according to inner region scalings, *i.e.* $u^+ = f(y^+)$. The laminar boundary layer's linear growth is again clearly visible, and follows the $u^+ = y^+$ law (shown in red dashes) over the entire boundary layer thickness. The velocity profile around the end of the transition region at $x/c = 0.71$ exhibits a viscous sub-layer until approximately $y^+ = 10$, and then closely follows the standard turbulent logarithmic law $u^+ = 2.44\log(y^+) + 5.2$ (blue dashes) until the outer region of the boundary layer at around $y^+ = 250$, although its slope appears to have a value slightly higher than 2.44. Inside the transition zone, velocity profiles are neither laminar, since mean velocity increases less than linearly with the distance from the wall, nor are they turbulent. In fact the velocity profiles appear to sweep the entire domain between the linear law and the log law as transition takes place, as also observed experimentally by Lee and Kang.[19]

Figure (5) represents rms turbulent streamwise velocity fluctuations measured at a height of $y^+ = 20$ along the upper boundary layer of the airfoil, plotted as a percentage of the free-stream velocity. Noticeable levels of fluctuations start to appear a little before $x/c = 0.5$, and they grow rapidly in amplitude to reach a saturation level of approximately 15% of free-stream velocity, at roughly $x/c = 0.75$. Their level then diminishes slightly, and flattens out approaching the trailing edge. The transition region thus commences in the vicinity of $x/c = 0.5$. The end of the transition zone is presumably close to the location after which the level of fluctuations starts to diminish, but the information given by this plot is not sufficient to place the zone's end with precision. However, these preliminary values are in good agreement with experimental data. For example, Lee and Kang[18] found the transition zones around a NACA 0012 airfoil at a Reynolds number of 600,000 and zero angle of attack to be located between $x/c = 0.62$ and $x/c = 0.78$, thanks to measurements performed by hot-wire anemometry. The transition zones are shorter than that on a flat plate at an equivalent Reynolds number, because of the presence of an adverse pressure gradient in this region

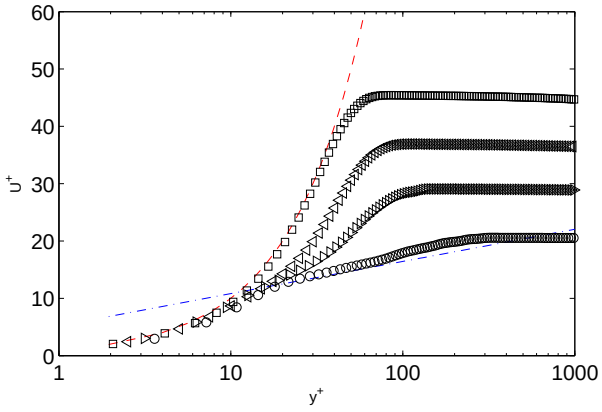

Figure 3. Velocity profiles plotted in wall units $u^+ = f(y^+)$ in the upper boundary layer around a NACA0012 airfoil at $\mathbf{Re}_c = 500,000$ and M= 0.22. - - - $u^+ = y^+$, - . - . - $u^+ = 2.44\log(y^+) + 5.2$, $\square$ $x/c = 0.52$, $\triangleleft$ $x/c = 0.59$, $\triangleright$ $x/c = 0.63$, $\circ$ $x/c = 0.71$.

created by the airfoil's geometry.

Figure (4) shows a colormap view of the rms streamwise velocity fluctuations around the transition zone. The vertical scale in this figure has been dilated by a factor of 10 in order to better show the region of interest. It can be seen in this view that the maximum levels of fluctuations are located between $x/c = 0.6$ and $x/c = 0.75$, which confirms the previous estimation of the transition zone's extent. This view of the rms fluctuations is in good qualitative agreement with similar plots presented in Kerho and Bragg[16] for a smooth NACA0012 airfoil at a Reynolds number of $\mathrm{Re}_c = 750,000$.

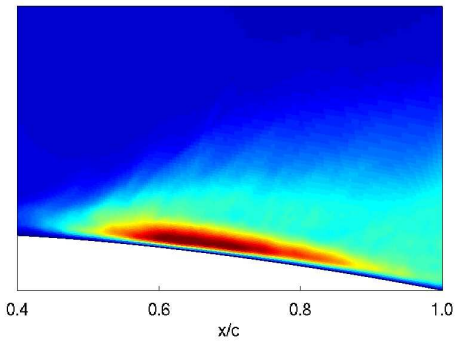

Figure 4. View of the rms streamwise velocity fluctuations around the transition zone on a NACA0012 airfoil at $\mathbf{Re}_c = 500,000$ and M= 0.22. Colour scale is between 0 and 15 percent of free stream velocity.

A better indication of the extent of the transition zone can be obtained from the variation in the local skin-friction coefficient $C_f = \tau_w/(0.5\rho U_\infty^2)$. Indeed, the skin friction coefficient in the laminar zone for a flat plate follows a different law from that in a turbulent zone. Figure (6) shows the skin friction coefficient obtained in this computation, for the central zone of the airfoil from 30% to 90% of the chord.

The minimum skin friction is reached around $x/c = 0.54$, after which point it rises rapidly to reach a maximum at about $x/c = 0.72$, before decreasing again towards the trailing edge. This places the transition zone's upstream and downstream bounds at $x/c \simeq 0.54$ and $x/c \simeq 0.72$ respectively.

A 2-D view of the ω_z vorticity field around the trailing edge of the airfoil, presented in Figure (7), gives a visual representation of the process of transition. The appearance of large-amplitude vortical disturbances is seen to take place very quickly, at approximately 63% of the chord in this snapshot.

Transversal rms fluctuation profiles of streamwise velocity are shown in Figure (8), measured at different points from the laminar zone down to the turbulent region.

Good qualitative and quantitative agreement in transversal turbulent fluctuation profiles is found be-

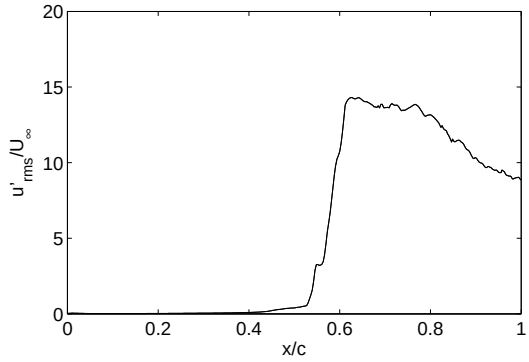

Figure 5. Velocity fluctuations u'_{rms}/U_∞ in the upper boundary layer around a NACA0012 airfoil at $\mathbf{Re}_c = 500,000$ and M= 0.22, calculated at $y^+ \simeq 16$, plotted as a function of x/c.

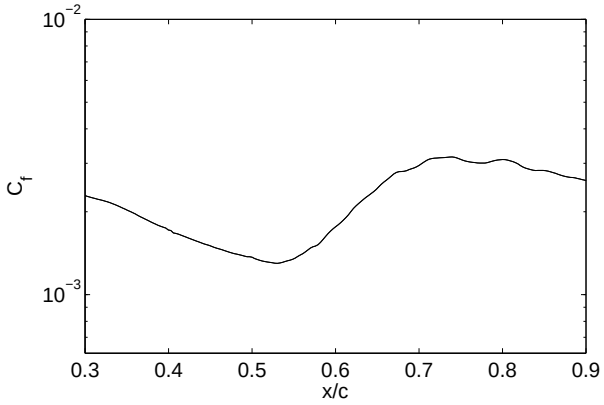

Figure 6. Skin friction around the transition zone of a NACA0012 airfoil at $\mathbf{Re}_c = 500,000$ and M= 0.22.

tween the computation and experimental results by Lee and Kang,[19] shown in Figure (9), although the computational values are slightly higher. The height at which the maximum fluctuation levels are reached is slightly lower in the computational results, at approximately $y^+ \simeq 25$, to be compared to the value of $y^+ \simeq 40$ obtained experimentally. The fluctuation profiles issued from the computation collapse cleanly in the viscous sublayer.

The progressive transition to a turbulent state can be observed in the time histories of the streamwise velocity signals shown in Figure (10). The first signal is measured at $x/c = 0.5$, the second is from inside the transition zone at $x/c = 0.63$, and the last plot is from the turbulent zone, at $x/c = 0.85$. All three signals are measured at a height of approximately 15 wall units from the airfoil. Note that the vertical scale for the first and last signal is half that of the second signal, in order to show signal shapes more clearly. Indeed, the second signal is measured at the point where maximum levels of rms fluctuations are observed in the boundary layer, as can be seen in Figures (4) and (5). It is interesting to note that the signal measured in the laminar zone is quite irregular. The oscillations are fairly sinusoidal, but their amplitude varies strongly with time.

The acoustic field generated by the airfoil is also captured and preserved in this computation. Figure (11) shows an instantaneous view of the fluctuating pressure around the airfoil. Sound waves can clearly be seen to radiate away from the trailing edge, the nearly circular aspect of these waves indicating that the emission zone is almost point-like. On this view, low amplitude sound waves can also be seen to be leaving the leading edge. The upstream flow has no turbulence, so it would appear that these waves are the result of the leading edge diffracting waves emitted at the trailing edge. Figure (12) shows a part of the time history of the fluctuating pressure at a distance of $y/c = 0.95$ above the trailing edge. In the fisrt portion of signal shown, there appears to be more high-frequency oscillations than the second. The power spectral

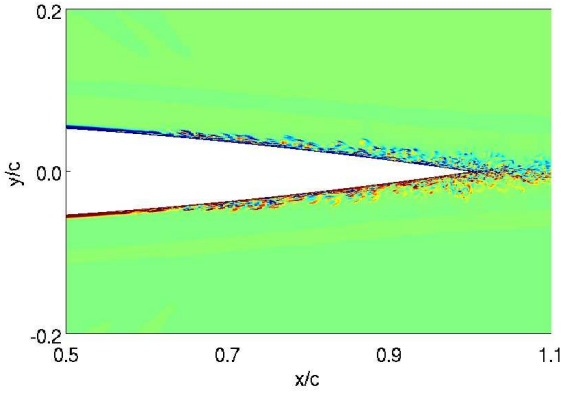

Figure 7. Instantaneous view of the ω_z vorticity in the boundary layers around the trailing edge of a 3D NACA 0012 airfoil at a Reynolds number of $\mathbf{Re}_c = 5 \times 10^5$ and M$= 0.22$. Colour scale is between $\pm 1 \times 10^5$.

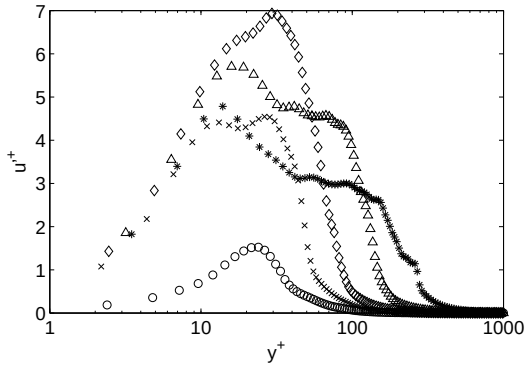

Figure 8. Velocity fluctuation profiles in the upper boundary layer around a NACA0012 airfoil: computation at $\mathbf{Re}_c = 500,000$ and M$= 0.22$. $\circ$ $x/c = 0.4$, $\times$ $x/c = 0.58$, $\diamond$ $x/c = 0.63$, $\triangle$ $x/c = 0.69$, $\star$ $x/c = 0.75$.

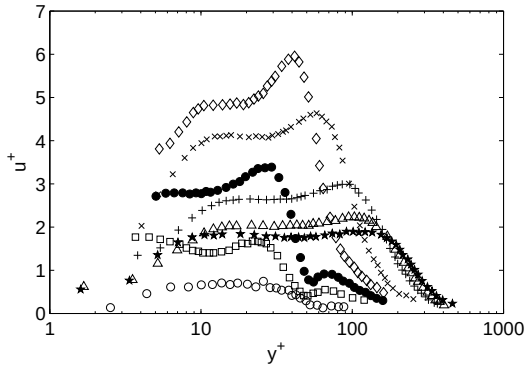

Figure 9. Velocity fluctuation profiles in the upper boundary layer around a NACA0012 airfoil at $\mathbf{Re}_c = 600,000$. Measurements by Lee and Kang. $\circ$ $x/c = 0.45$, $\square$ $x/c = 0.58$, $\bullet$ $x/c = 0.62$, $\diamond$ $x/c = 0.65$, $\times$ $x/c = 0.68$, $+$ $x/c = 0.72$, $\triangle$ $x/c = 0.75$, $\star$ $x/c = 0.78$.

density of the fluctuating pressure measured at this location is shown in Figure (13). The main maximum is located at a frequency of roughly 21kHz, and is relatively wide, stretching approximately from 15 to 28kHz. This band of frequencies corresponds to those of the large-amplitude velcoity fluctuations present at the beginning of the transition zone. Indeed, these structures have an average length of approximately 2.2 mm. If we assume an average convection velocity, from the transition region to the trailing edge, of $U_c = 0.7U_\infty$,

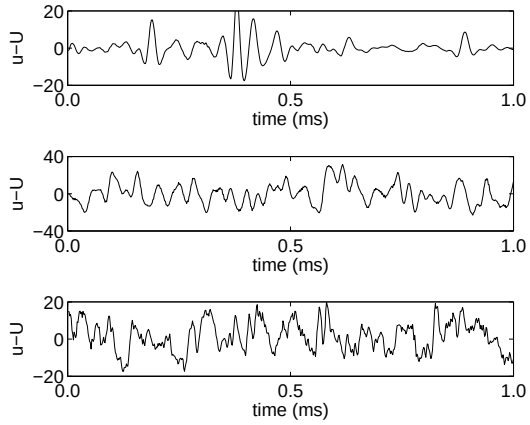

Figure 10. Velocity signals at different points along the boundary layer.

then the 2.2mm structures cross the trailing edge at a frequency of about 23.5kHz. The aforementioned high-frequency component visible in the first half of Figure (12) corresponds to the peak in the spectrum at about 100kHz. Data is currently being examined to ascertain the origin of this high-frequency peak. However, it can be noted that there is no indication of a strongly tonal Tollmien-Schlichting (T-S) type acoustic radiation present in Figure (13). This is in agreement with experimental observations by McAlpine *et al.*[23] for a NACA0012 airfoil at a Reynolds number of 340,000 and at zero incidence to the flow. They observed a laminar to turbulent transition shortly upstream of the trailing edge, and concluded that this transition broke any possible T-S feedback loop, thus precluding tonal noise.

Spanwise correlation of the acoustic field reaches a value of 1 very quickly after leaving the boundary layer. This is not surprising, given the small spanwise extent of the computational domain with respect to typical transversal acoustic correlation lengths found experimentally.

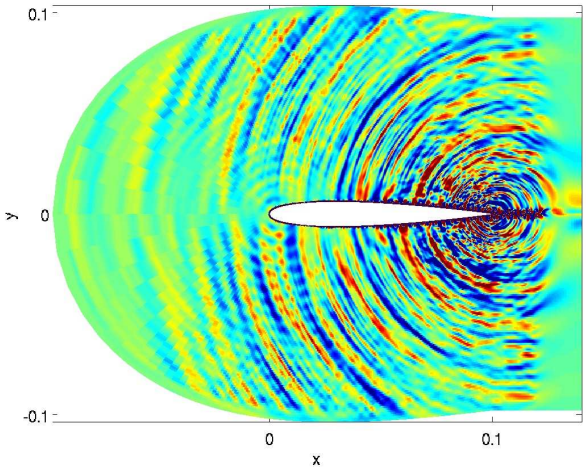

Figure 11. Snapshot of the fluctuating pressure field around a NACA0012 airfoil at $\mathbf{Re}_c = 500,000$. Colour scale is between -5 and 5 Pa.

IV. Conclusions

The flow around a 3D NACA0012 airfoil at a transitional chord-based Reynolds number of 500,000 and a Mach number of 0.22 has been studied numerically, with a parallel curvilinear compressible solver based on high-order methods. The airfoil is placed in a uniform mean flow, parallel to the direction of the flow. At

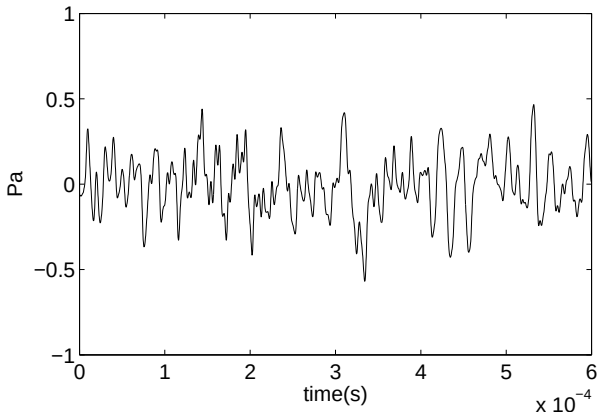

Figure 12. Time history of the fluctuating pressure at the edge of the computational domain above the trailing edge of a NACA0012 airfoil.

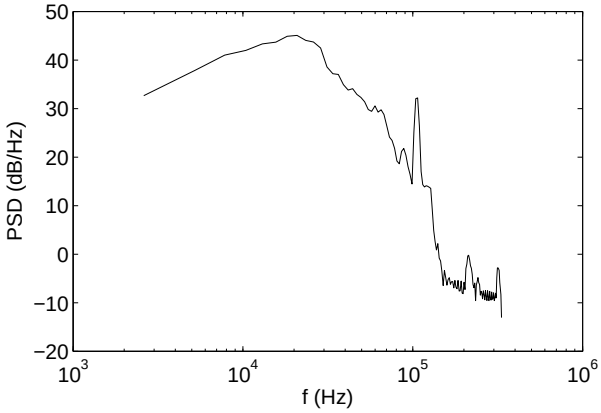

Figure 13. Power spectral density of the fluctuating pressure signal of Figure (12).

this Reynolds number, experimental studies indicate that the airfoil's boundary layers are initially laminar, and transition to a turbulent state along the second half of the airfoil. The computational results show that the location of the transition zone is well captured, and that the mean velocity field after the transition region is well described by the standard turbulent logarithmic law. Furthermore, rms velocity fluctuation profiles and skin friction values are in good agreement with experimental data.

The acoustic field resulting from turbulent boundary layer structures crossing the trailing edge is also obtained in the same computation. First analyses of the acoustic data indicate that it follows expected trends. A broadband radiation pattern is observed, and no tonal Tollmien-Schlichting feedback loop is detected.

It is hoped in the near future to perform similar computations at different Mach numbers, allowing to check the scaling of the acoustic power with Mach number.

References

[1]J. Berland, C. Bogey, and C. Bailly, *Optimized explicit schemes: Matching and boundary schemes, and 4th-order runge-kutta algorithm*, AIAA Paper 2004-2814 (2004).

[2]D.J. Bodony and S.K. Lele, *On using large-eddy simulation for the prediction of noise from cold and heated turbulent jets*, Phys. Fluids **17** (2005), no. 085103-1.

[3]C. Bogey and C. Bailly, *Three-dimensional non-reflective boundary conditions for acoustic simulations : far field formulation and validation test cases*, Acta Acustica **88** (2002), no. 4, 463–471.

[4]_____, *A family of low dispersive and low dissipative explicit schemes for noise computations*, J. Comput. Phys. **194** (2004), no. 1, 194–214.

[5]_____, *Computation of a high reynolds number jet and its radiated noise using large eddy simulation based on explicit filtering*, Computers and Fluids (2006), to appear.

[6]C. Bogey, C. Bailly, and D Juvé, *Noise investigation of a high subsonic, moderate Reynolds number jet using a compressible LES*, Theoretical and Computational Fluid Dynamics **16** (2003), no. 4, 273–297.

[7]F.H. Clauser, *Turbulent boundary layers in adverse pressure gradients*, Journal of the Aeronautical Sciences **21** (1954), no. 2, 91–108.

[8]S. Dahlström and L. Davidson, *Large eddy simulation of the flow around an airfoil*, AIAA Paper 2001-0425 (2001).

[9]_____, *Large eddy simulation applied to a high-reynolds flow around an airfoil close to stall*, AIAA Paper 2003-0776 (2003).

[10]L. Davidson, D. Cokljat, J. Fröhlich, M.A. Leschziner, C. Mellen, and W. Rodi, *LESFOIL: Large eddy simulation of the flow around a high-lift airfoil*, Notes on Numer. Fluid Mech., Springer **83** (2003).

[11]R.L. Evans, *Freestream turbulence effects on turbulent boundary layers in adverse pressure gradients*, AIAA Journal **23** (1985), no. 11, 1814–1816.

[12]V.M. Falkner and W. Skan, *Some approximate solutions of the boundary layer equations*, A.R.C Reports and Memoranda (1930), no. 1314.

[13]X. Gloerfelt, C. Bailly, and D. Juvé, *Direct computation of the noise radiated by a subsonic cavity flow and application of integral methods*, J. Sound Vib. **266** (2003), no. 1, 119–146.

[14]R. Hixon, M. Nallasamy, and S.D. Sawyer, *Parallelization strategy for an explicit computational aeroacoustics code*, AIAA Paper 2002-2583 (2002).

[15]J.A. Hoffman, S.M. Kassir, and S.M. Larwood, *The influence of free-stream turbulence on turbulent boundary layers with mild adverse pressure gradients*, NASA Contractor Report (1989), 177520.

[16]M.F. Kerho and M.B. Bragg, *Airfoil boundary-layer development and transition with large leading-edge roughness*, AIAA Journal **35** (1997), no. 1.

[17]H.-J. Kim, S. Lee, and Fujisawan N., *Computation of unsteady flow and aerodynamic noise of naca0018 airfoil using large-eddy simulation*, International Journal of Heat and Fluid Flow (2005), disponible en ligne.

[18]H.K. Lee and S.H Kang, *Flow characteristics of transitional boundary layer on the NACA0012 airfoil in wakes*, Proceedings of FEDSM'98, Washington, DC (1998).

[19]_____, *Flow characteristics of transitional boundary layers on an airfoil in wakes*, Journal of Fluids Engineering **122** (2000), no. 3, 522–532.

[20]H. Ludwieg and W. Tillmznn, *Investigations of the wall shearing stress in turbulent boundary layers*, NACA T.M. (1950), no. 1285.

[21]E. Manoha, C. Herrero, P. Sagaut, and S. Redonnet, *Numerical prediction of airfoil aerodynamic noise*, AIAA Paper 2002-2573 (2002).

[22]O. Marsden, C. Bogey, and C. Bailly, *High-order curvilinear simulations of flows around non-cartesian bodies*, J. Comput. Acous. **13** (2005), no. 4, 731–748.

[23]A. McAlpine, E.C. Nash, and M.V. Lowson, *on the generation of discrete tones by the flow around an aerofoil*, J. Sound Vib. **222** (1999), no. 5, 753–779.

[24]C. Mellen, J. Fröhlich, and W. Rodi, *Lessons from the European LESFOIL project on LES of flow around an airfoil*, AIAA Paper 2002-0111 (2002).

[25]A. Oberai, F. Roknaldin, and Th. Hughes, *Computation of trailing-edge noise due to turbulent flow over an airfoil*, AIAA Journal **40** (2002), no. 11, 2206–2216.

[26]J.-H. Seo and Y. Moon, *Perturbed compressible equations for aeroacoustic noise prediction at low mach numbers*, AIAA Journal **43** (2005), no. 8.

[27]S.E. Sherer and M. Visbal, *Computational study of acoustic scattering from multiple bodies using a high-order overset grid approach*, AIAA Paper 2003-3203 (2003).

[28]C.K.W. Tam and Z. Dong, *Radiation and outflow boundary conditions for direct computation of acoustic and flow disturbances in a nonuniform mean flow*, J. Comput. Acous. **4** (1996), no. 2, 175–201.

[29]A. Uzun, G. Blaisdell, and A. Lyrintzis, *3-d large eddy simulation for jet aeroacoustics*, AIAA Paper 2003-3322 (2003).

[30]M. Visbal and D. Gaitonde, *Very high-order spatially implicit schemes for computational acoustics on curvilinear meshes*, J. Comput. Acous. **9** (2000), no. 4, 1259–1286.

[31]M. Wang and P. Moin, *Computation of trailing-edge flow and noise using large-eddy simulation*, AIAA Journal **38** (2000), no. 12, 2201–2209.